

# ACCURATE MODELING OF TAGGED CMR 3D IMAGE APPEARANCE CHARACTERISTICS TO IMPROVE CARDIAC CYCLE STRAIN ESTIMATION

Matthew Nitzken<sup>1</sup>, Garth Beach<sup>2</sup>, Ahmed Elnakib<sup>1</sup>, Fahmi Khalifa<sup>1</sup>, Georgy Gimel'farb<sup>3</sup>, Ayman El-Baz<sup>1</sup>

<sup>1</sup>BioImaging Laboratory, Bioengineering Department, University of Louisville, Louisville, KY, USA.

<sup>2</sup>Radiology Department, School of Medicine, University of Louisville, Louisville, KY, USA.

<sup>3</sup>Department of Computer Science, University of Auckland, Auckland, New Zealand.

## ABSTRACT

To reduce noise within a tag line, unsharpen the tag edges in spatial domain, and amplify the tag-to-background contrast, a 3D energy minimization framework for the enhancement of tagged Cardiac Magnetic Resonance (CMR) image sequences, based on learning first- and second-order visual appearance models, is proposed. The first-order appearance modeling uses adaptive Linear Combinations of Discrete Gaussians (LCDG) to accurately approximate the empirical marginal probability distribution of CMR signals for a given sequence, and separates tag and background submodels. It is also used to classify the tag lines and the background. The second-order model considers image sequences as samples of a translation- and rotation-invariant 3D Markov-Gibbs Random Field (MGRF) with multiple pairwise voxel interactions. A 3D energy function for this model is built by using the analytical estimation of the spatiotemporal geometry and Gibbs potentials of interaction. To improve the strain estimation, by enhancing the tag and background homogeneity and contrast, the given sequence is adjusted using comparisons to the energy minimizer. Special 3D geometric phantoms, motivated by statistical analysis of the tagged CMR data, have been designed to validate the accuracy of our approach. Experiments with the phantoms and eight real data sets have confirmed the high accuracy of the functional parameters that are estimated for the enhanced tagged sequences when using popular spectral techniques, such as spectral Harmonic Phase (HARP).

**Index Terms**— Tagged CMR image, tag line, linear combination of Gaussians, Markov random field, appearance model.

## 1. INTRODUCTION

Tagged Cardiac Magnetic Resonance Imaging (CMR) is a well-known technique for detailed and non-invasive visualization of myocardium motion and deformation [1]. Local diseases, such as coronary atherosclerosis, and global conditions, such as heart failure and diabetes, result in wall dysfunction that manifest on tagged images, with full 3D spatial geometric concordance. Cardiac, or MR, tagging, places a pre-specified pattern of temporary markers (called tags) inside soft body tissues, e.g. tag lines created by patterns of magnetic spin in the examined tissue, so that the motion in the tagged tissue can be measured from the images [2]. This technique complements traditional anatomical images and can capture detailed information about the heart over time. The tag lines allow for computing displacement, velocity, rotation, elongation, strain, and twist of the heart. While traditional MR techniques carry only information about the motion at the boundaries of an object, the tag lines allow us to examine the strain and displacement of the interior of the tissue in close detail [3].

Known methods for analyzing tagged MR images fall into two broad categories: spatial and frequency, or spectral, domain ones. The former identify and use spatial locations of the tag lines in an image to estimate the whole tissue motion and strain using either model-based or model-free interpolation and differentiation [4]. An established spectral Harmonic Phase (HARP) method, from the second category, computes phase images from sinusoidal tagged MR images by applying bandpass filters in the Fourier domain. The tissue motion field is built then by the HARP tracking that is based on the fact that harmonic phases of material points do not change with motion [5, 6].

Our research aims to improve the reliability of methods based on spectral domain analysis. HARP analysis, and other very efficient spectral algorithms for quantitative tag analysis, are often hampered by image noise that affects spatial tag profiles [7], and when this occurs the assumed motion invariance of the harmonic phases of material points does

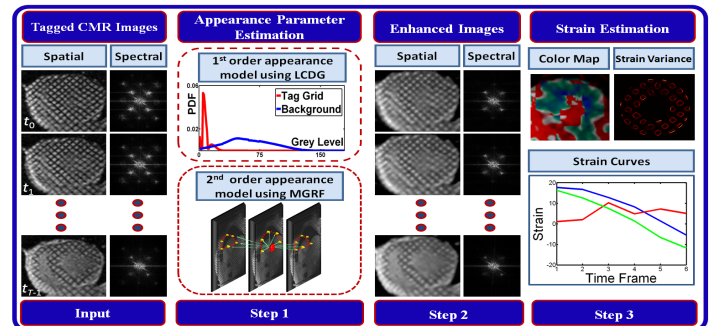


Fig. 1. Block-diagram of the proposed refinement of tagged MR images.

not hold. The HARP tracking may also fail at points that are close to the tissue boundary, and at points approaching or leaving the image plane due to through-plane motion. The failures caused by corrupted images may require the user to manually identify and correct the mistracked points. This is a very time-consuming process, especially in a research study or a clinical examination when large numbers of data points must be tracked. Because optimum tagged cardiac MR images are difficult to obtain, effective image refining and correcting techniques are a prime necessity. To perform the tag data extraction we use the commercial HARP analysis package *Diagnosoft*.

Several techniques have been proposed to directly improve tagged MR images. For example, Yang and Murase [1] proposed a technique to improve tagged MR images based on contrast enhancement and texture analysis. Their technique uses an automatic segmentation of the left ventricle in 2D tagged MR images. Histogram modification and local contrast enhancement are then used to improve the contrast between tagged lines and non-tagged tissue. In a continuation of the first paper, Yang and Murase [8] use a refined method that incorporates additional filtering before applying the histogram equalization. To recover missing data found between tag lines Yuan et al. [9] proposed an approach for the implementation of a complex bandpass filter using wavelet decomposition. Evaluation of the technique by the authors showed that while this technique did provide enhancement to the taglines it was difficult to efficiently employ the algorithm.

Additionally, a number of techniques have been proposed to improve the HARP tracking algorithms. Khalifa et al. [10] proposed a method for improving the motion tracking of tagged cardiac MR images. Their method presents an improvement to the robustness of traditional HARP tracking methods by combining standard HARP tracking with active contour models. A similar technique, by Tecelao et al. [11], also proposes a technique to improve HARP tracking through modification of the traditional HARP tracking algorithm. This approach seeks to solve the corruption problem by using modified K-Space filtering along with HARP angle computations to improve the tracking of points. Cordero-Grande et al. [12] proposed an alternative technique that focuses on integrating a windowed Fourier transform in the HARP tracking algorithm.

Liu et al. [7] proposed a HARP tracking refinement that is based on using a seeded region growing technique. This technique seeks to solve the problems associated with image motion by starting from a user-defined seed point which is determined to be correctly tracked throughout the entire sequence. The method is expanded upon by Liu et al. [2] to incorporate additional methods, namely flood-filling, to help reduce errors. This technique is initialized by a user-defined reference selection and

synthetic tags are introduced to help to improve the accuracy of through plane motion tracking. An alternative method proposed by Spottiswoode et al. [13] also uses a form of phase unwrapping and temporal fitting to improve the tracking of tag points in DENSE image sets.

In summary the above techniques generally suffer from the following problems: (i) the majority of techniques focus on either improving the HARP tracking algorithm directly, which makes compatibility with existing commercial HARP frameworks difficult if not impossible, or (ii) focus on improving the contrast of tag lines in the image spatial representations, which does not reliably adjust the spectral qualities; (iii) the majority of techniques require some form of user input or prior knowledge, which can be time consuming difficult to acquire; and (iv) the techniques that modify the images directly are computationally expensive.

To address the problem of tagged MR image refinement we propose a more practicable energy minimization based approach for improving the tagged CMR images directly. In our approach, the image noise is reduced and the tag-to-background contrast is enhanced using an original 3D energy function, which accounts for spatiotemporal pairwise signal interactions, and accurate voxel-wise classification by modeling marginal probability distributions of tag and background signals. The energy function is derived from a probabilistic first- and second-order prior appearance model of the tagged CMR image sequences. Shown in Fig. 1, the stages of the proposed approach are detailed below.

## 2. IMAGE REFINEMENT: MODELS AND METHODS

**Basic notation.** Let  $\mathbf{r} = (x, y, t)$  and  $\mathbf{R} = [(x, y, t) : x = 0, \dots, X - 1; y = 0, \dots, Y - 1, t = 0, \dots, T - 1]$  denote a 3D point, or voxel with two spatial ( $x, y$ ) and one time ( $t$ ) coordinates and a spatiotemporal lattice of the size  $XYT$ , respectively. Let  $\mathbf{Q} = \{0, \dots, Q - 1\}$  be a finite set of signals (i.e., gray levels intensities). The lattice  $\mathbf{R}$  supports 3D CMR image sequences  $\mathbf{g} = [g(x, y, t) : (x, y, t) \in \mathbf{R}; g(x, y, t) \in \mathbf{Q}]$ , consisting of 2D MR slices taken in successive time instants.

We describe visual appearance of the tagged CMR images with a 1<sup>st</sup>-order model of marginal probability distributions of tag and background signals and a 2<sup>nd</sup>-order model of characteristic voxel-wise and pairwise voxel signal dependencies. The latter are modeled with a generic translation and rotation invariant central-symmetric Markov-Gibbs random field (MGRF) with pairwise voxel potentials depending on signal differences.

### 2.1. The 2<sup>nd</sup>-Order MGRF Appearance Model

A translation- and rotation-invariant generic second-order MGRF of images  $\mathbf{g}$  is specified by a certain number,  $N$ , of characteristic central-symmetric voxel neighborhoods  $\mathbf{n}_\nu; \nu = 1, \dots, N$ , on  $\mathbf{R}$  shown in Fig. 2. Each neighborhood  $\mathbf{n}_\nu$  indicates a family of voxel pairs,  $\mathbf{C}_\nu = \{\mathbf{c}_\nu = (\mathbf{r}, \mathbf{r}') : \mathbf{r}' - \mathbf{r} \in \mathbf{n}_\nu; \mathbf{r}, \mathbf{r}' \in \mathbf{R}\}$ , such that the inter-voxel distances (norms of the coordinate offsets  $\mathbf{o} = \mathbf{r}' - \mathbf{r}$ ) belong to an indexed semi-open interval  $[d_{\nu:\min}, d_{\nu:\max}]$ :

$$d_{\nu:\min} \leq \sqrt{(x - x')^2 + (y - y')^2 + (t - t')^2} < d_{\nu:\max}. \quad (1)$$

with the fixed thresholds  $d_{\nu:\min}$  and  $d_{\nu:\max}$ . These neighboring pairs are considered as second-order cliques of the neighborhood graph with nodes in the voxels.

Cliques from the family  $\mathbf{C}_\nu$  support the same real-valued Gibbs potential  $V_\nu(\mathbf{g}(\mathbf{r}), \mathbf{g}(\mathbf{r}'))$  of pairwise voxel interaction. To uniformly account for contrast, the potential depends on the absolute intra-clique signal difference:  $\Delta = |g(\mathbf{r}) - g(\mathbf{r}')| \in \mathbf{D} = \{0, 1, \dots, Q - 1\}$ . The potential values can be represented as a vector  $\mathbf{V}_\nu = [V_\nu(\Delta) : \Delta \in \mathbf{D}]^\top$  where  $\top$  indicates the transposition. The characteristic cliques to be taken into account in the MGRF are stratified into  $N$  families,  $\{\mathbf{C}_\nu : \nu = 1, \dots, N\}$ , with the potentials  $\mathbf{V}_\nu$  and non-intersecting distance intervals:  $d_{1:\min} < d_{1:\max} \leq d_{2:\min} < \dots \leq d_{N:\min} < d_{N:\max}$ .

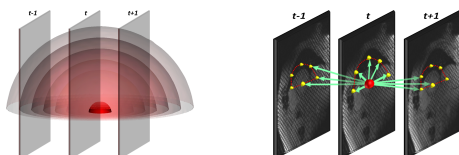


Fig. 2. Central-symmetric 2<sup>nd</sup>-order 3D neighborhood system for a voxel.

Such an MGRF has the Gibbs probability distribution [14]:

$$P(\mathbf{g}) = \frac{1}{Z} \exp \left( |\mathbf{R}| \left( \mathbf{V}_{\text{vox}}^\top \mathbf{F}(\mathbf{g}) + \sum_{\nu=1}^N \rho_\nu \mathbf{V}_\nu^\top \mathbf{F}_\nu(\mathbf{g}) \right) \right) \quad (2)$$

where  $Z$  is the normalizing factor (the partition function) depending on the potentials  $\mathbf{V} = [\mathbf{V}_{\text{vox}}; \mathbf{V}_\nu : \nu = 1, \dots, N]$  and the neighborhoods  $\{\mathbf{n}_\nu : \nu = 1, \dots, N\}$ , and  $\rho_\nu = \frac{|\mathbf{C}_\nu|}{|\mathbf{R}|}$  is the relative size of the clique family with respect to the lattice cardinality  $|\mathbf{R}| = XYT$ , i.e., the relative number of cliques in the family  $\mathbf{C}_\nu$ . The vectors  $\mathbf{F}(\mathbf{g})$  and  $\mathbf{F}_\nu(\mathbf{g})$  contain relative empirical frequencies  $f(q|\mathbf{g})$  of signals  $q \in \mathbf{Q}$  in the voxels and frequencies  $f_\nu(\Delta|\mathbf{g})$  of absolute signal differences  $\Delta \in \mathbf{D}$  in the cliques from the family  $\mathbf{C}_\nu$  for the image  $\mathbf{g}$ , respectively:

$$\begin{aligned} \mathbf{F}(\mathbf{g}) &= \left[ f(q|\mathbf{g}) = \frac{|\mathbf{R}_q(\mathbf{g})|}{|\mathbf{R}|}; \sum_{q \in \mathbf{Q}} f(q|\mathbf{g}) = 1 \right] \\ \mathbf{F}_\nu(\mathbf{g}) &= \left[ f_\nu(\Delta|\mathbf{g}) = \frac{|\mathbf{C}_{\nu:\Delta}(\mathbf{g})|}{|\mathbf{C}_\nu|}; \sum_{\Delta \in \mathbf{D}} f_\nu(\Delta|\mathbf{g}) = 1 \right] \end{aligned}$$

where the sublattice  $\mathbf{R}_q(\mathbf{g})$  contains all the voxels  $\mathbf{r}$ , such that  $g(\mathbf{r}) = q$  and the subfamily  $\mathbf{C}_{\nu:\Delta}(\mathbf{g})$  contains all the cliques  $\mathbf{c}_\nu = (\mathbf{r}, \mathbf{r}')$  of this family, such that  $|g(\mathbf{r}) - g(\mathbf{r}')| = \Delta$ .

Analytical first approximations of the maximum likelihood estimates of the potentials in line with [14] are as follows:

$$\begin{aligned} V_{\text{vox}}(q) &= \lambda (f(q|\mathbf{g}) - f_{\text{irf}}(q)); q \in \mathbf{Q}; \\ V_\nu(\Delta) &= \lambda (f_\nu(\Delta|\mathbf{g}) - f_{\text{irf}}(\Delta)); \Delta \in \mathbf{D}; \nu = 1, \dots, N \end{aligned} \quad (3)$$

where the common scaling factor  $\lambda$  is also computed analytically, and  $f_{\text{irf}}(q) = \frac{1}{Q}$  and  $f_{\text{irf}}(\Delta)$  denote the probability of the signal  $q$  and the inter-voxel signal difference  $\Delta$ , respectively, for the independent random field of equiprobable signals:

$$f_{\text{irf}}(\Delta) = \begin{cases} \frac{1}{Q} & \text{if } \Delta = 0 \\ \frac{2(Q-\Delta)}{Q^2} & \text{otherwise} \end{cases}$$

The factor  $\lambda$  can be omitted ( $\lambda = 1$ ) if only relative interaction energies  $E_{\text{rel}:\nu}$  are computed for the clique families to select the most characteristic ones.

### 2.2. The 1<sup>st</sup>-Order LCDG Appearance Model

A discrete Gaussian (DG)  $\Psi_\theta = (\psi(q|\theta) : q \in \mathbf{Q})$  is defined [15] as a discrete probability distribution with  $Q$  components obtained by integrating a continuous 1D Gaussian density  $\varphi(q|\theta) = (\sigma * \sqrt{2\pi})^{-1} * \exp\left(-\frac{(q-\mu)^2}{2\sigma^2}\right)$  with parameters  $\theta = (\mu, \sigma)$ , where  $\mu$  is the mean and  $\sigma^2$  is the variance, over  $Q$  intervals related to the successive signal values in  $\mathbf{Q}$ : if  $\Phi_\theta(q) = \int_{-\infty}^q \varphi(z|\theta) dz$  is the cumulative Gaussian probability function, then  $\psi(0|\theta) = \Phi_\theta(0.5)$ ,  $\psi(q|\theta) = \Phi_\theta(q + 0.5) - \Phi_\theta(q - 0.5)$  for  $q = 1, \dots, Q - 2$ , and  $\psi(Q-1|\theta) = 1 - \Phi_\theta(Q - 1.5)$ .

To enhance the tag-to-background contrast, the empirical marginal 1D signal distribution for the CMR image to be refined is accurately approximated with a Linear Combination of Discrete Gaussians (LCDG)  $\mathbf{P}_{\mathbf{w}, \Theta} = [p_{\mathbf{w}, \Theta}(q) : q \in \mathbf{Q}]; \sum_{q \in \mathbf{Q}} p_{\mathbf{w}, \Theta}(q) = 1$ , with two positive dominant and multiple sign-alternate subordinate DGs:

$$p_{\mathbf{w}, \Theta}(q) = \sum_{k=1}^{K_p} w_{p:k} \psi(q|\theta_{p:k}) - \sum_{l=1}^{K_n} w_{n:l} \psi(q|\theta_{n:l}) \quad (4)$$

where  $K_p; K_p \geq 2$ , and  $K_n; K_n \geq 0$ , are total numbers of the positive and negative DGs, and  $\mathbf{w} = [w_{p:k}, w_{n:l}]$  are the non-negative weights that meet the obvious constraint  $\sum_{k=1}^{K_p} w_{p:k} - \sum_{l=1}^{K_n} w_{n:l} = 1$ . The subordinate DGs approximate closely the deviations of the empirical distribution from the conventional mixture of the dominant positive DGs.

This initial LCDG model is built and separated into the two LCDG submodels of the tag lines and their background, respectively, with the Expectation-Maximization(EM) based techniques introduced in [15] such that the misclassification rate is minimal.

### 2.3. Energy Minimization to Enhance Tagged CMR Images

We adjust a tagged CMR image  $\mathbf{g}$  by searching with the voxel-wise Iterative Conditional Mode (ICM) relaxation for a local minimum of the Gibbs energy function for the second-order MGRF appearance model:

$$\hat{\mathbf{g}} = \arg \min_{\mathbf{g} \in \mathbf{Q}^{X \times Y \times T}} \left\{ \mathbf{V}_{\text{vox}}^T \mathbf{F}(\mathbf{g}) + \sum_{\nu=1}^N \rho_\nu \mathbf{V}_\nu^T \mathbf{F}_\nu(\mathbf{g}) \right\} \quad (5)$$

where the probability vectors  $\mathbf{F}_{\text{vox}}(\mathbf{g})$  and  $\mathbf{F}_\nu(\mathbf{g})$  are collected over the generated tagged CMR image sequence. To enhance the tag-background contrast, each estimated signal value  $\hat{g}(\mathbf{r})$ ;  $\mathbf{r} \in \mathbf{R}$ , is classified as belonging to either the tag line or the background by using the first-order LCDG modelling. Then the voxels are nudged towards their proper grouping by incrementing or decrementing their signals by a small value  $\delta$  in accord with the discriminant threshold,  $\tau$ .

Basic steps of the proposed enhancement are as follows:

1. Find the empirical marginal probability distribution by normalizing the signal histogram collected over a given tagged CMR image sequence.
2. Use the LCDG modeling of Section 2.2 to estimate the LCDG submodels approximating the marginal signal distributions for the tag lines and the background.
3. Use these LCDG-submodels to evaluate the discriminant threshold  $\tau$ , which minimizes the error of classification of the tag and background voxels by their signal values.
4. For the given sequence, use Eq. (3) in Section 2.1 to estimate the first- and second-order potentials.  $\mathbf{V}_{\text{vox}}$  and  $\mathbf{V}$ , of the MGRF appearance model.
5. Starting from the given sequence  $\mathbf{g}$ , use the ICM to estimate a sequence  $\hat{\mathbf{g}}$ , which minimizes the energy of Eq. (5).
6. Compare the estimated voxel signals  $\hat{g}(\mathbf{r})$ ;  $\mathbf{r} \in \mathbf{R}$ , to the threshold  $\tau$  found at Step 3 and add the bias  $\delta$  to or subtract the bias  $\delta$  from the estimated gray level value if the latter is greater or lesser than the threshold, respectively.

## 3. EXPERIMENTAL RESULTS

The effectiveness of the proposed approach was tested on both synthetic phantom images and in-vivo data by analyzing the strain of the data sets using the HARP technique and quantifying the performance with two indexes: (i) the ability to restore strain slopes for synthetic phantoms and (ii) the homogeneity of the strain variance in the data.

### 3.1. Validation on Synthetic Phantoms

The synthetic phantoms were constructed using a descriptive mathematical model [16] that accounts for physiological features and the left ventricle (LV) response during the cardiac cycle. To obtain the phantoms, a motion transformation is applied to a generated 3D LV model. Then, an image is generated by selecting an image plane that intersects the LV and assigning every point on the image plane a value that depends on whether the point lies inside or outside the LV wall. A phantom constructed using this model is exemplified in Fig. 3 (a). Realistic images are simulated by corrupting the phantom images with Gaussian noise using the signal-to-noise Ratios (SNR) of 3.18 dB and 2.58 dB, as shown in Fig. 3 (b) and (c), respectively.

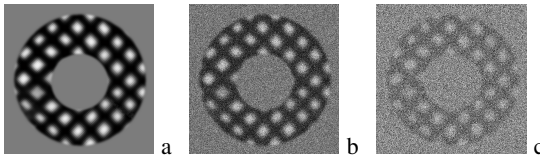


**Fig. 3.** Original phantom (a) and two Gaussian corruption levels with the SNR of 3.18 dB (b) and 2.58 dB (c).

In cardiac strain analysis, the slope of the contraction phase of the cardiac cycle is a very important part of the strain curve, i.e., cardiac systolic performance index, or rate of peak contraction. Therefore, the accurate recovery of this slope is an important index of a tagged MR restoration algorithm. To measure the effect of the additive noise on the calculated strain, the absolute strain error, i.e., the difference between the slopes

of the noisy data analyzed and the ground truth, was calculated for the phantom images, using the HARP technique and the Euler strain measurements. The absolute strain error for the noisy phantom images has been reduced after the proposed processing from 94% to 35.7%. Figure 4 visually compares the strain in the original, corrupted, and enhanced phantom images.

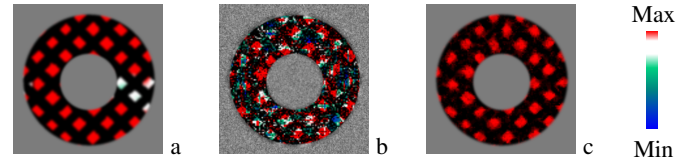


**Fig. 4.** Visualization of the strain on the phantom for the original (a), corrupted (b) and enhanced (c) images. Coloring indicates the strain percentage. Note how the strain is largely recovered in the enhanced image.

The actual strain slopes calculated for the original, noisy, and our enhanced phantoms are compared in Fig. 5. As is expected and demonstrated in Fig. 5, the strain values are decreasing linearly with time during the contraction phase of the cardiac cycle. That the slope profiles for the enhanced and ground truth images are very similar clearly demonstrates the capabilities of the proposed approach to facilitate the accurate recovery of the strain slopes for the tagged MR data. Visually this is also evident from the color uniformity of the images in Fig. 4, (a) and (c). At the same time, the color scatter over the noisy phantom in Fig. 4, (b), illustrates the failure of the HARP-based strain calculations under the large corrupting noise.

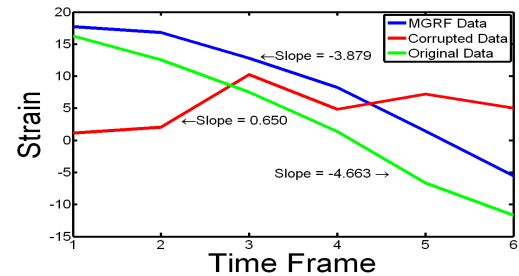


**Fig. 5.** Strains calculated at the contraction phase of the cardiac cycle for the original, corrupted, and enhanced phantom images. Note that the slope is made unreliable, and does not approximate the actual underlying data in the corrupted phantom, indicating that the HARP analysis cannot track the strain at all in this image. After applying our enhancement to the corrupted image, the slope, is largely recovered.

For accurate computations in the spectral domain, the HARP technique requires that the information reside predominately within the central peak and first side lobes. The Fourier spectral representations of the noisy and enhanced phantom images in Fig. 6 justify the high accuracy of recovering the strain slope using the proposed approach. As shown in Fig 6 (a), it is the increased power scatter distributing information in the outer side lobes of the Fourier domain for the noisy phantom image that greatly affects the accuracy of the HARP analysis [17].

On the contrary, our enhancement reduces the scatter in the outer side lobes and emphasizes the main lobe and first side lobes in the Fourier image spectral domain, which therefore makes the HARP analysis much more accurate. In total, our approach gives  $265\% \pm 20\%$  of noise reduction in the side lobes of the phantom image spectrum. Table 1 summarizes the noise reduction results for the phantom data.

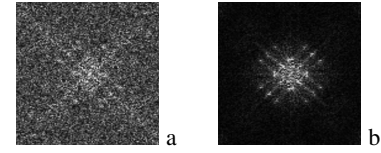


**Fig. 6.** Fourier spectra of the noisy (a) and enhanced (b) phantom images.

Another important aspect of the proposed approach is the ability to restore strain homogeneity in the tagged MR images, which is directly related to the ability to restore the strain slopes (the improved homogeneity leads to the improved strain slope). Based on biomechanical models of the heart tissue as a continuous material, neighboring voxels in a heart should

have similar strains, and the strain does not randomly occur in every individual voxel, the variance in strain (homogeneity) in actual tagged MR image sequences should be low[18]. This should hold true in any given continuous region, even in the presence of injury. To justify our approach, after the strains of each image were extracted, the strain homogeneity of the phantoms was calculated in terms of the strain variance in  $7 \times 7$  windows across the phantom images. Differences between the mean strain homogeneity in Table 2 before and after the image enhancement are statistically significant by the unpaired  $t$ -test, so that our approach robustly improves both the strain slope and homogeneity.

Spectral Ratio	Before	After	Before	After
	Phantom		In-vivo	
	Mean	0.17	0.58	1.40
St.dev.	0.012	0.019	0.19	0.31
% mean imp.	<b>265%</b>	<b>45.52%</b>		

**Table 1.** Showing the ratio of the main lobe's spectral power for the phantom data set before (noisy) and after processing and the 20 in-vivo data sets before and after processing, with the percentage of improvement..

	Before	After
Mean	0.024	0.0092
St.dev.	$2.9 \cdot 10^{-14}$	$1.8 \cdot 10^{-15}$
P-Value		$< 10^{-4}$

**Table 2.** Phantom strain homogeneity before and after processing.

To illustrate this result, pixel-wise parametric (color-coded) maps in Fig. 7 for the original, noisy, and enhanced phantoms are used to help visually assess the improvement in the strain homogeneity: the brighter the area, the larger the local strain variance. Our approach largely recovers the strain variance profile of the original image.

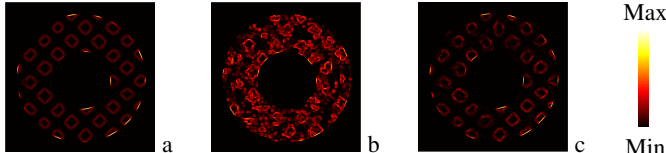


**Fig. 7.** Color-coded strain variance maps for the original (a), noisy (b), and enhanced (c) phantom. The corrupted image shows an increased amount of variance and less discrete elements.

### 3.2. Results for In-vivo Data

To test the realistic performance, the proposed approach has been applied to eight in-vivo data sets. Shown in Fig. 8, the results before and after enhancing one of the test images are similar to those for the phantom data, and the spectra shows a considerable noise reduction in the side lobes; see Fig. 8 (c) and (d).

As shown in Table 1, the proposed approach can significantly reduce various levels of the noise, e.g., the noise reduction of  $42.6\% \pm 9.3\%$  in the spectral side lobes for all the eight in-vivo data sets that take part in these experiments. Furthermore, similarly to the phantom data, the overall strain homogeneity of the image clearly increases as well. Figure 9 demonstrates the color strain maps for an in-vivo image before and after the proposed enhancement, showing improved continuous areas.

### 3.3. Computational Efficiency

The processing time of the entire HARP analysis is only slightly increased with the proposed approach and for a  $256 \times 256$  DICOM image typically takes  $9.4 \pm 0.2$  seconds to process, while a typical data set, of 15 MR images, was on average 145 seconds. Unlike other alternatives, our technique requires no user input or apriori model templates, reduces the overall data analysis time, and makes the analysis more robust due to the elimination of possible human errors.

## 4. CONCLUSION

Spectral techniques, such as HARP, are arguably the most clinically useful image processing techniques for the fast analysis of cardiac strain data. While many approaches have been proposed to improve tagged MR images as a whole, only a few of them have focused directly on improving the quality of images in order to directly facilitate spectral analysis. Our results show that probabilistic first- and second-order models of spatiotemporal images can contribute directly to image denoising in the spectral domain, and therefore improve these spectral techniques.

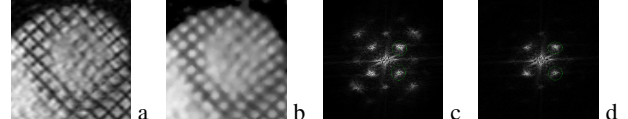


**Fig. 8.** An in-vivo data set: the original spatial (a) and processed (b) images and their Fourier spectra (c), (d). The spectral noise is notably reduced by the proposed image enhancement.

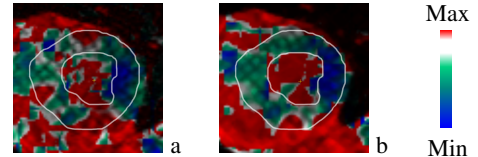


**Fig. 9.** In-vivo data strain maps before (a) and after (b) our enhancement. Note that the variability in strain has been largely reduced and the final homogeneity is notably increased.

Our LCDG and MGRF based modeling of the tagged MR images in the spatiotemporal domain is capable of recovering strain slopes, improving the main-to-side-lobe ratio in the Fourier spectra, and improving the strain homogeneity of the image. These image improvements ensure a more efficient and robust estimation of functional parameters with the today's spectral tools. In total, our approach adds only a minimal amount of time to HARP image analysis and leads to more accurate clinical cardiac measurements and evaluations, which provides clinicians with more accurate image data

## 5. REFERENCES

- [1] X. Yang and K. Murase, "Tagged cardiac mr image segmentation by contrast enhancement and texture analysis," in *IEEE ICEMI*, pp. 4–210 –4–214, Aug 2009.
- [2] X. Liu and J. Prince, "Shortest path refinement for motion estimation from tagged mr images," *IEEE TMI*, vol. 29, no. 8, pp. 1560 –1572, Aug 2010.
- [3] L. Axel and L. Dougherty, "MR imaging of motion with spatial modulation of magnetization," *Radiology*, vol. 171, pp. 841–845, Jun 1989.
- [4] M. Ledesma-Carbayo *et al.*, *Fully Automatic 3D Cardiac Tagged MRI Analysis using Multiple Source Non-Rigid Registration Techniques*, 2009, p. 1814.
- [5] N. F. Osman and J. L. Prince, "Visualizing myocardial function using HARP MRI," *Phys Med Bio*, vol. 45, pp. 1665–1682, Jun 2000.
- [6] B. A. Venkatesh, *et al.*, "Three-dimensional plus time biventricular strain from tagged MR images by phase-unwrapped harmonic phase," *J of Magn Reson Im*, vol. 34, pp. 799–810, Oct 2011.
- [7] X. Liu, E. Murano *et al.*, "Harp tracking refinement using seeded region growing," in *IEEE ISBI*, pp. 372 –75, April 2007.
- [8] X. Yang and K. Murase, "A multi-scale phase-based optical flow method for motion tracking of left ventricle," in *IEEE iCBME*, pp. 1–4, June 2010.
- [9] X. Yuan, *et al.*, "A multiresolution method for tagline detection and indexing," *IEEE ITiB*, vol. 14, no. 2, pp. 507 –513, Mar 2010.
- [10] A. Khalifa, A. Youssef *et al.*, "Improved harmonic phase (harp) method for motion tracking a tagged cardiac mr images," *IEEE EMBS*, pp. 4298 –4301, Jan 2005.
- [11] S. Tecelao, *et al.*, "Extended harmonic phase tracking of myocardial motion: improved coverage of myocardium and its effect on strain results," *J of Magn Reson Im*, vol. 23, pp. 682–690, May 2006.
- [12] L. Cordero-Grande, *et al.*, "Improving harmonic phase imaging by the windowed fourier transform," in *IEEE ISBI*, pp. 520–3, Apr 2011
- [13] B. Spottiswoode, X. Zhong *et al.*, "Tracking myocardial motion from cine dense images using spatiotemporal phase unwrapping and temporal fitting," *IEEE TMI*, vol. 26, no. 1, pp. 15 –30, Jan 2007.
- [14] G. Gimel'farb, *Image textures and Gibbs random fields*. Kluwer Academic Pub, 1999, vol. 16.
- [15] A. El-Baz and G. Gimel'farb, "Em based approximation of empirical distributions with linear combinations of discrete gaussians," in *IEEE ICIP*, vol. 4, pp. 373–376, Oct 16–19 2007.
- [16] E. Waks, J. Prince *et al.*, "Cardiac motion simulator for tagged mri," in *IEEE MMBIA*, , pp. 182 –191, Jun 1996.
- [17] K. Hansen, F. Gran *et al.*, "In-vivo validation of fast spectral velocity estimation techniques," *Ultrasonics*, vol. 50, no. 1, pp. 52 –59, 2010.
- [18] K. B. Chandran, *et al.*, *Image-Based Computational Modeling of the Human Circulatory and Pulmonary Systems*. Springer, 2010.